Materials Advances

ROYAL SOCIETY OF CHEMISTRY

PAPER

View Article Online
View Journal | View Issue

Cite this: *Mater. Adv.*, 2025, 6, 2925

An integrated computational and experimental study of BSA-coated $MnFe_2O_4$ nanoparticles as a drug delivery platform for quercetin

Negin Hashemi,[ab] Shabnam Naderlou,[a] Ali Mohammadi[ab] and Hossein Danafar *[ab]

Quercetin, a bioactive flavonoid with limited bioavailability, was investigated using BSA-coated $MnFe_2O_4$ nanoparticles as a novel delivery system. An integrated computational and experimental approach was employed, combining DFT calculations and molecular docking simulations to analyze quercetin's interactions with the $MnFe_2O_4$ surface across (011), (101), and (100) facets, alongside *in vitro* studies to assess drug loading and release, biocompatibility, and cytotoxicity on 4T1 cells. Molecular docking showed favorable binding energies between quercetin and BSA (−5.17 kcal mol^{-1} with Subdomain IIA), demonstrating that quercetin, even when bound to the BSA coating, retained strong interactions with the oxide surface. Reduced density gradient (RDG) analysis revealed facet-dependent adsorption mechanisms, correlating binding affinity towards Mn (through oxygen-containing functional groups) with steric interactions shown as red areas on the RDG plot. Analysis unveiled the interactions and structural features of each facet of the drug complex. Experimentally, the TEM imaging revealed the nanoparticles to possess a spherical morphology with an average diameter of around 7 nanometers and the average size of nanoparticles by DLS is 85.27 ± 0.26 nm with a PDI of 0.25. The BSA coating improved drug loading to 27.5% and resulted in a dose-dependent cytotoxic effect on 4T1 tumor cells. Specifically, a release of 62% of the loaded quercetin was observed at pH 5.7 after 120 hours, compared to only 41% at pH 7.4. The *in vitro* assessment also demonstrated high biocompatibility, with less than 5% hemolysis observed at concentrations up to 200 μg mL^{-1}. *In vivo* studies show no mouse death in the test of LD_{50}. Overall, these findings support the potential of BSA-coated $MnFe_2O_4$ nanoparticles as a promising drug delivery platform to enhance quercetin's stability and bioavailability for effective tumor growth inhibition.

Received 20th February 2025,
Accepted 23rd March 2025

DOI: 10.1039/d5ma00161g

rsc.li/materials-advances

1. Introduction

Cancer remains one of the foremost causes of mortality globally.[1] Breast cancer, the most prevalent malignancy among women, poses a major threat to their health and well-being.[2] Historically, various methods have been employed to tackle this challenging disease, including surgical intervention, chemotherapy (CT), and radiation therapy (RT). While these conventional treatments are effective, they have limitations that have compelled scientists to explore novel combination therapies with fewer side effects on healthy cells compared to traditional treatments.[3] The BALB/c mouse strain is widely used in cancer research, because of its inherent susceptibility to tumorigenesis and its genetic resemblance to humans.[4] To further investigate the potential of novel cancer therapies, researchers have turned to chemodynamic therapy (CDT), a promising approach that leverages Fenton and Fenton-like reactions to combat cancerous cells.[5] This innovative cancer therapy utilizes endogenous hydrogen peroxide (H_2O_2) within tumor cells to generate highly reactive oxygen species (ROS), such as hydroxyl radicals (•OH), singlet oxygen ($^1O_2$), peroxides (O_2^{2-}) and superoxide anions (O_2^-), derived from the incomplete reduction of oxygen (O_2).[6] These reactive molecules target critical components of cancerous cells, including DNA, proteins, and cell membranes, ultimately leading to cellular damage and death.[7,8]

Bimetallic $MnFe_2O_4$ nanoparticles, as photosensitizers, display enhanced biocompatibility compared to other metal oxides, establishing them as promising candidates for a range of biomedical applications, including drug delivery and magnetic resonance imaging (MRI).[8] To effectively induce oxidative stress and trigger apoptosis in tumor cells, a high generation level of ROS is essential. However, the presence of intracellular antioxidants

[a] *Zanjan Pharmaceutical Biotechnology Research Center, Zanjan University of Medical Sciences, Zanjan, Iran. E-mail: danafar@zums.ac.ir; Fax: +98 241 4273639; Tel: +98 241 4273635*
[b] *Department of Pharmaceutical Nanotechnology, School of Pharmacy, Zanjan University of Medical Sciences, Zanjan, Iran*

such as glutathione (GSH) poses a significant challenge by reducing ROS levels and limiting the efficacy of CDT.[9] The synthesis and design of metal-based nanocomposites, particularly $MnFe_2O_4$, can optimize cancer therapy and promote ROS production through iron ions, which act as a catalyst. Furthermore, $MnFe_2O_4$ nanoparticles are recognized for their ability to serve as a heat source in cancer treatment through the process of magnetic hyperthermia, as they generate heat when exposed to alternating magnetic fields.[10] $MnFe_2O_4$ nanoparticles have emerged as promising candidates for drug delivery applications due to their unique combination of properties. Their superparamagnetic nature allows for targeted delivery to tumor sites under an external magnetic field, enhancing drug accumulation and reducing systemic side effects.[11] Furthermore, $MnFe_2O_4$ nanoparticles can be used to induce localized hyperthermia, generating heat that can selectively kill cancer cells.[12] Compared to other metal oxides, $MnFe_2O_4$ exhibits relatively good biocompatibility, which can be further enhanced through surface modification with biocompatible materials such as bovine serum albumin (BSA).[13] The high surface area of $MnFe_2O_4$ nanoparticles also facilitates efficient drug loading, enabling the delivery of therapeutic doses of quercetin.[8] Finally, $MnFe_2O_4$'s redox activity can be harnessed for chemodynamic therapy, generating reactive oxygen species (ROS) within the tumor microenvironment.[14] These combined properties make $MnFe_2O_4$ nanoparticles an attractive platform for targeted and controlled quercetin delivery. Bovine serum albumin (BSA) is a protein extracted from the plasma of cattle. It is frequently utilized as a coating for nanoparticles across a range of biomedical applications, including drug delivery, diagnostics, and imaging techniques.[15] The use of BSA-coated nanoparticles presents a promising strategy to improve both the efficacy and safety of drug delivery systems.[16]

Numerous organic and inorganic nanomaterials, such as hydrogels, biopolymers, liposomes, gold and silver nanoparticles, and carbon nanotubes, have been the subject of extensive research aimed at exploring their efficacy in the realm of cancer therapy.[17–21] Despite the breadth of investigation into these materials, a significant number of them are encumbered by various constraints, notably issues concerning inadequate drug retention and unpredictable release patterns.[22] Quercetin (3,5,7,3′,4′-pentahydroxyflavanone) is a polyphenol found in health foods and plant-based products, with applications in the food, cosmetic, and pharmaceutical industries due to its therapeutic potential. Despite favorable roles in cancer therapy, such as impacting cell signaling pathways, its chemical instability, low aqueous solubility, and short biological half-life limit its clinical use.[23] Quercetin's therapeutic potential has spurred the investigation of various nanoparticle-based delivery systems, including liposomes,[24] polymeric nanoparticles,[25] and metal nanoparticles.[26] However, these systems often suffer from limitations such as low drug loading capacity, burst release profiles, and limited targeting specificity.[27] Therefore, there is a need for novel quercetin delivery systems that address these limitations and enhance its therapeutic efficacy. These limitations underscore the critical need for further refinement and innovation in the development of nanomaterial-based approaches to cancer treatment.[25–28] Nanoparticle delivery systems address these challenges by increasing solubility and dissolution rates due to their high surface area and good adhesion to biological surfaces.[29]

Targeting cancerous cells is facilitated by several distinctive characteristics of tumor cells. First, leveraging the Enhanced Permeability and Retention (EPR) effect facilitates the extravasation and accumulation of nanoparticles in tumors and increases the permeability characteristics of tumor blood vessels.[11] Additionally, the acidic environment surrounding tumors promotes iron ion release, further enhancing therapeutic efficacy.[30] The acidic nature of the tumor microenvironment (TME), characterized by a pH of approximately 6.5,[31] significantly influences the release of iron ions. This reduced pH level stimulates the release of both ferrous (Fe^{2+}) and ferric (Fe^{3+}) ions within the tumor. The heightened availability of these iron ions in the acidic TME subsequently promotes the generation of highly reactive oxygen species (ROS) through Fenton and Fenton-like reactions. This localized increase in ROS can destroy cancer cells by inducing oxidative stress and ultimately triggering apoptosis. Thus, the intrinsic acidity of the TME establishes conditions conducive to iron-mediated mechanisms of cell death.[32] Furthermore, combination therapies can improve the efficacy of individual modalities while minimizing adverse effects. Monotherapy with either CT or RT frequently results in substantial psychological and physical side effects. The concurrent application of CDT, CT, and RT can yield synergistic benefits, thereby enhancing treatment outcomes and potentially reducing side effects. CDT and quercetin can potentially enhance ROS production; also, ionizing radiation during RT contributes to ROS generation.[33] Additionally, quercetin plays a crucial role in modulating cellular signaling pathways involved in proliferation and survival, such as PI3K/Akt[34] and MAPK pathways.[35] Moreover, RT can induce DNA damage by activating DNA damage response pathways and promoting cell mortality.[36] Chen *et al.* also proposed comprehensive strategies for CDT and developed multimodal anticancer therapies based on CDT techniques.[37] Xu *et al.* developed a multifunctional nanoplatform utilizing a tannic acid-iron network loaded with doxorubicin (DOX) to facilitate combined chemotherapy and chemodynamic therapy.[38] To optimize the design of BSA-coated $MnFe_2O_4$ nanoparticles for quercetin delivery, a comprehensive understanding of the drug–nanoparticle interactions at the molecular level is essential.

Computational modeling techniques, including density functional theory (DFT) calculations and molecular docking simulations, provide valuable insights into binding affinities, interaction mechanisms, and adsorption preferences on different crystal facets.[39] In particular, the Reduced Density Gradient (RDG) method allows for a detailed analysis of non-covalent interactions, revealing steric and hydrogen bonding contributions to drug adsorption. These computational studies, complemented by *in vitro* experiments assessing drug loading, release kinetics, cytotoxicity, and biocompatibility, offer a holistic approach to evaluate the potential of this nanosystem for

cancer therapy. In this study, we employed an integrated computational and experimental approach to investigate the interaction of quercetin with BSA-coated $MnFe_2O_4$ nanoparticles. DFT and molecular docking simulations were conducted to examine the adsorption mechanisms of quercetin on the $MnFe_2O_4$ (011), (101), and (100) facets, while *in vitro* experiments evaluated drug loading capacity, release behavior, and cytotoxic effects on 4T1 tumor cells. By elucidating the molecular and structural characteristics of quercetin adsorption, this research provides crucial insights into the design of efficient $MnFe_2O_4$-based drug delivery systems, paving the way for enhanced quercetin bioavailability and targeted cancer therapy. While various nanoparticle-based delivery systems have been explored for quercetin, they often suffer from limitations such as low drug loading capacity, burst release profiles, and limited targeting specificity. In contrast, our study presents a novel approach that combines BSA-coated $MnFe_2O_4$ nanoparticles with a detailed computational analysis of facet-specific quercetin binding. This unique combination allows us to achieve enhanced drug loading, pH-responsive release, improved biocompatibility, and targeted delivery. Furthermore, we validate the therapeutic potential of our system through combined chemotherapy and radiotherapy. By addressing the limitations of existing quercetin delivery methods, our study offers a promising new strategy for enhancing the therapeutic efficacy of quercetin in cancer treatment.

2. Materials and methods

2.1 Experimental methods

2.1.1. Materials. Manganese chloride tetrahydrate ($MnCl_2{\cdot}4H_2O$) and iron(III) chloride ($FeCl_3$) were sourced from Merck in Germany, and BSA, ammonia solution (NH_4OH) and quercetin were acquired from Sigma-Aldrich in USA. The 4T1 cell line, a murine mammary carcinoma model, was obtained from the Pasteur Institute cell bank in Tehran. MTT was procured from Atocel in Austria, and phosphate-buffered saline (PBS) was purchased from Inoclon in Iran. Ethanol was supplied by Merck in Germany.

2.1.2. Preparation of $MnFe_2O_4$ nanoparticles. Manganese ferrite ($MnFe_2O_4$) nanoparticles were prepared using a co-precipitation method. The synthesis involved manganese chloride tetrahydrate ($MnCl_2{\cdot}4H_2O$) and iron(III) chloride ($FeCl_3$) as precursors, with the ammonia solution (NH_4OH) serving as the precipitating agent. Initially, 348 mg of $MnCl_2{\cdot}4H_2O$ (a molecular weight of 197.9 g mol^{-1}) and 143.53 mg of $FeCl_3$ (a molecular weight of 162.2 g mol^{-1}) were completely dissolved in deionized water, maintaining a molar ratio of 2 : 1. Following this, an 8 M NH_4OH solution was added gradually to the homogenous mixture using a micropipette while ensuring continuous magnetic stirring. To achieve the desired pH range of 9–12, an additional 6 M NH_4OH was introduced. The aging period was crucial in influencing both the precipitation process and the resultant particle size. Following precipitation, the solid was separated by centrifugation at 13 000 rpm for 20 min and underwent ten washing cycles. The resulting material was then dried in an oven at 80 °C for 72 hours(h) to facilitate the complete formation of the manganese ferrite phase. The final dried product comprised the targeted $MnFe_2O_4$ nanoparticles.

2.1.3. Preparation of $MnFe_2O_4$@BSA nanoparticles. To make BSA-coated $MnFe_2O_4$ nanoparticles, we first dissolved 250 mg of BSA protein (purchased from Sigma-Aldrich, with a molecular weight of 66.5 kDa) in 8 mL of water. Then, we slowly added 50 mg of $MnFe_2O_4$ nanoparticles to the solution. The mixture was allowed to stabilize at room temperature for 30 min and then incubated for an additional 12 h to facilitate the coating process. Following incubation, the resulting BSA-coated nanoparticles were purified through dialysis (with a membrane pore size of 12 kDa) against deionized water, with the water being replaced every four hours for 48 h, to remove unbound BSA and other impurities.

2.1.4. Fourier-transform infrared (FTIR) analysis. FT-IR spectroscopy was employed to verify the successful synthesis of the nanoparticles and to investigate their interactions. A Tensor 27 FT-IR spectrometer (Bruker, Biotage, Germany) was used to examine the vibrational modes of the nanoparticles.

2.1.5. Transmission electron microscopy (TEM) analysis. TEM was utilized to perform both quantitative and qualitative elemental analyses, in addition to assessing the crystallographic structure and orientation of components down to 30 nanometers in size. The morphology and dimensions of the samples were investigated using a Cambridge 360-1990 Stereoscan TEM, which was equipped with an energy-dispersive X-ray spectroscopy (EDS) system for enhanced elemental characterization.

2.1.6. X-ray diffraction (XRD) analysis. XRD analysis was performed utilizing Cu Kα radiation (λ = 1.542 Å) to collect data over an angular range of 20 to 80 degrees, using a Bruker AXS D8 Advance diffractometer (Germany and United States).

2.1.7. Investigating the hydrodynamic size of nanoparticles. The zeta potential and size distribution of nanoparticles were ascertained by the Dynamic Light Scattering (DLS) methodology using a Nano Zetasizer (Nano ZS90, Malvern Instruments), with the results documented in a graphical format. The zeta potential of the nanoparticle surface and the carriers was similarly evaluated utilizing DLS apparatus. To facilitate this process, the initially prepared samples were diluted to attain the requisite absorption range suitable for DLS assessments, subsequently allowing for the determination of the dimensions of the prepared nanoparticles *via* the DLS device.

2.1.8. Ultraviolet-visible (UV-vis) analysis. UV-vis spectrophotometry is a method that relies on the absorption of light by a substance or an unknown sample. Each substance has a distinct interaction with light, leading to a unique UV-vis spectrum for each one. This spectrum serves as a valuable tool for both identifying and quantitatively analyzing various substances. For this study, a Thermo Scientific BioMate 5 spectrophotometer was utilized.

2.1.9. Preparation of quercetin loaded nanoparticles. To load quercetin onto the newly developed nano-hybrids, we

began by dissolving 5 mg of quercetin in 2 mL of ethanol. This solution was then carefully added dropwise to an aqueous suspension containing the nanocarrier, which comprised 20 mg of $MnFe_2O_4$@BSA nanoparticles. Following the drug loading process, centrifugation was employed to isolate any unloaded quercetin.

2.1.10. Determination of the amount of quercetin loaded on $MnFe_2O_4$@BSA. To assess the amount of quercetin *via* UV-vis spectrophotometry at 375 nm, a calibration curve was established. Initially, 2.2 mg of quercetin was dissolved in 1 mL of acetone. From this solution, 200 μL was combined with 1800 μL of PBS buffer in a ratio of 65 : 35. Subsequently, 10 μL of the resultant mixture was further diluted with 990 μL of buffer. The absorbance at 375 nm was measured three times. This process was repeated six additional times for concentrations of 2.2, 4.4, and 8.8 μg mL^{-1}. To facilitate the analysis, a calibration curve of concentration *versus* absorbance was generated using Microsoft Excel 2016, and the data's goodness of fit was evaluated by reporting the linear equation and the correlation coefficient.

2.1.11. Quercetin release behavior of $MnFe_2O_4$@BSA–quercetin nanoparticles. To examine the quercetin release behavior of $MnFe_2O_4$@BSA–quercetin nanoparticles during dialysis under two distinct pH conditions (7.4 and 5.7), 2 mL of $MnFe_2O_4$@BSA–quercetin was encapsulated in a dialysis bag (a membrane cut-off of 12 kDa). The dialysis bag was subsequently submerged in 15 mL of phosphate-buffered saline (PBS) solution at pH 7.4 within a shaking incubator set to 37 °C and 100 rpm. At specified time intervals, 1 mL of the external solution surrounding the dialysis bag was extracted, and an equivalent volume of buffer maintaining the corresponding pH was promptly refilled into the incubator. The absorbance of the collected samples was then measured at 375 nm utilizing a UV-vis spectrophotometer.

2.1.12. Hemolysis assay. To evaluate the biocompatibility and effects of synthesized nanoparticles ($MnFe_2O_4$@BSA–quercetin and $MnFe_2O_4$@BSA) on red blood cells, a study was undertaken. Red blood cells were subjected to varying concentrations (50, 100, and 200 μg mL^{-1}) of these nanoparticles. Blood was collected from a volunteer, and an anticoagulant was added to prevent clotting. Subsequently, red blood cells were isolated from the plasma and thoroughly washed to eliminate any residual plasma components. The washed red blood cells were incubated at 37 °C for 5 hours with the different nanoparticle concentrations, along with distilled water (serving as a negative control) and phosphate-buffered saline (PBS, serving as a positive control). After incubation, the samples underwent centrifugation, and the supernatant was collected. The absorbance of the supernatant was measured at 540 nm using a microplate reader, allowing for the calculation of hemolysis percentage based on these absorbance values. A higher percentage of hemolysis indicates greater damage to the red blood cells.

$$\text{Hemolysis (\%)} = \frac{(A_s - A_b)}{(A_p - A_b)} \times 100$$

2.1.13. Assessment of cytotoxic effects on cancerous cells. In this experiment, 7000 4T1 cells were plated in each well of a 96-well plate and allowed to incubate for 24 h, facilitating cell attachment. Following this incubation, the cells were subjected to a specific treatment and then were treated with quercetin-loaded nanoparticles at different concentrations of 20, 60 and 80 μg mL^{-1} and an equivalent amount of carrier, and the free medium was considered as the control group and subsequently exposed to radiation therapy. The cells were then incubated for an additional 24 h to allow the effects of the treatment and radiation to manifest. To evaluate cell viability, an MTT assay was conducted. 10 μL of MTT solution (5 mg mL^{-1}) was introduced into each well and incubated for 4 h. After this incubation period, 100 μL of DMSO was added to each well, and the absorbance was measured at 570 nm to determine cell viability. The MTT assay serves as an indicator of cell metabolic activity. Viable cells metabolize the yellow tetrazolium salt MTT into purple formazan crystals, with the amount of formazan produced directly proportional to the number of living cells present.

2.1.14. LD_{50} assay. *In vivo* safety assessment of developed $MnFe_2O_4$@BSA–quercetin nanoparticles was performed using the median lethal dose (LD_{50}). In this test, BALB/c female mice (~20 g weight) as an animal model were used to determine the possible *in vivo* toxicity of synthesized nanoparticles. Accordingly, $MnFe_2O_4$@BSA–quercetin at various concentrations ranging from 25 to 150 mg kg^{-1} was administrated to the mice by intravenous injection (n = 4 mice per dose). To determine the LD_{50}, the body weight and survival rate of mice were then monitored for three weeks. Also, blood indexes were analyzed on the first, 14th, and 28th day posttreatment with $MnFe_2O_4$@BSA–quercetin.

2.2. Computational methods

In order to account for facet-dependent interactions, we constructed slab models representing three different crystallographic orientations of $MnFe_2O_4$: the (100), (101), and (111) facets. These facets were chosen because they represent the most commonly exposed surfaces in $MnFe_2O_4$ nanoparticles synthesized under typical conditions and are also known to be thermodynamically stable.[40] Furthermore, these facets exhibit distinct surface properties, including variations in surface energy, atomic arrangement, and availability of binding sites, which may significantly influence their interaction with quercetin and BSA. By examining these specific facets, we aim to provide insights into the facet-dependent adsorption mechanisms that govern quercetin loading and release. Fig. 1 presents models of $MnFe_2O_4$. While spherical models better represent the overall morphology of nanoparticles, our layered (slab) theoretical modeling approach was chosen to isolate and analyze the surface interactions critical for adsorption. The slab model allows for detailed investigation of adsorption geometries, binding energetics, and electronic structure modifications at the interface, providing insights that are directly translatable to real-world applications. These slab models were chosen to capture the diversity of adsorption sites available on

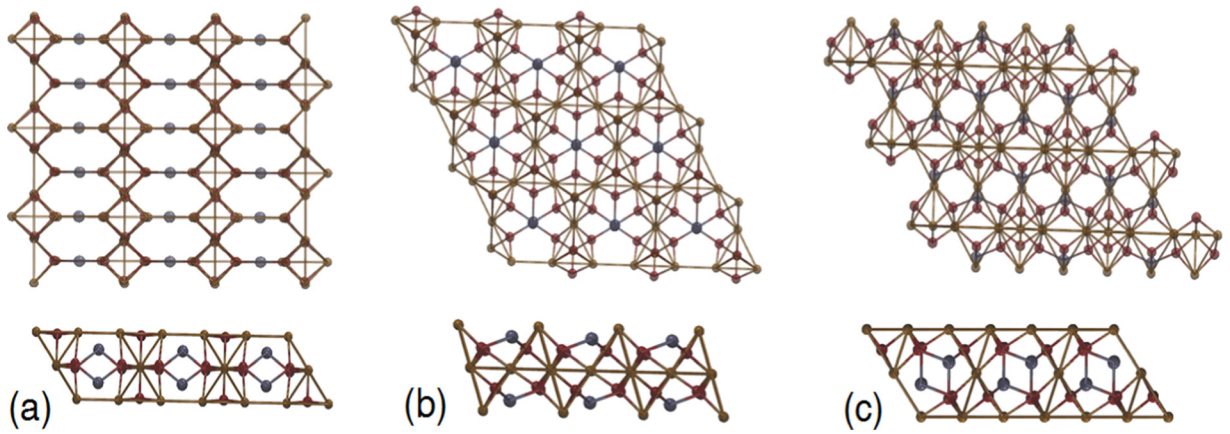

Fig. 1 Schematic representation of slab models for $MnFe_2O_4$ facets used in this study. The figure illustrates the three distinct surface orientations: (100) (a), (101) (b), and (011) (c). In the schematic, the (100) facet is shown as a relatively flat surface with moderate coordination (a), the (101) facet exhibits a higher density of exposed metal sites (b), and the (011) facet displays a more corrugated topology (c). These models form the basis for DFT and molecular docking studies of quercetin adsorption.

the nanoparticle surface, as the local atomic arrangement can significantly influence binding strength and electronic properties. Each slab model was constructed with a vacuum layer of 15–20 Å to eliminate interactions between periodic images. Mercury,[41] Avogadro,[42] Gaussview5.0.8,[43] and VMD[44] software programs were used to create graphical visualizations. Detailed descriptions of the calculation methods are provided in subsequent sections.

2.2.1 Molecular docking. Molecular docking simulations were performed using AutoDock4[45] to predict the binding orientations and affinities of quercetin on both the BSA protein and the $MnFe_2O_4$ surfaces. This process provided initial binding poses that were further refined using DFT geometry optimization. The crystal structure of BSA was obtained from the Protein Data Bank (PDB ID: 4F5S).[46] The structure was prepared for docking by removing water molecules and any co-crystallized ligand. Polar hydrogens were added to the protein using AutoDock Tools. Prior to docking, the geometry of quercetin was optimized using the ORCA quantum chemistry software.[47] A second-order Møller–Plesset perturbation theory (MP2) method with the aug-cc-pVTZ basis set[48] was employed. The optimized structure of quercetin was then prepared for docking by adding hydrogen atoms and electrostatic potential (ESP) fitting utilizing the ChelpG[49] method for charges. The ligand was treated as flexible with all its torsions being rotatable. $MnFe_2O_4$ surfaces were generated from slab models representing the (100), (101), and (011) facets. These optimized slab models were then used to build surface models for molecular docking. For the partial atomic charges of the $MnFe_2O_4$ structures, RESP[50] fitting using the REPEAT[51] method was utilized. Prior to docking quercetin, the optimized $MnFe_2O_4$ surfaces representing the (100), (101), and (011) facets were individually docked into BSA. This was done to explore how $MnFe_2O_4$ interacts with BSA separately and to create the BSA–$MnFe_2O_4$ complex as a basis for further docking studies. In order to study the interaction of quercetin with BSA before the presence of $MnFe_2O_4$, we separately docked the optimized structure of quercetin into the binding site of BSA. To assess potential ternary interactions, we then docked quercetin into the most stable complex resulting from previous docking simulations where $MnFe_2O_4$ interacted with BSA. The grid box encompassing the binding pocket was defined based on the known binding sites for metals and quercetin[52–54] and had dimensions of 60 Å × 60 Å × 60 Å, with a grid point spacing of 0.375 Å. The Lamarckian genetic algorithm (LGA) was used to perform the docking simulation with a population size of 250, a maximum of 2 500 000 energy evaluations, and a maximum of 27 000 generations. 100 independent docking runs were conducted. The best docked pose was selected based on the lowest binding energy score. The resulting complexes were visually inspected using PyMol[55] and UCSF Chimera[56] software's.

2.2.2. Density Functional Theory (DFT) Calculations. To study the interaction between quercetin and different facets of $MnFe_2O_4$, periodic DFT calculations were performed using the CP2K code.[57] The Quickstep module[58] was used for the electronic structure calculations, which employed a combination of Gaussian-type orbitals (GTOs) and plane wave (PW) methods.[59] The rev-PBE exchange–correlation functional was used along with the D3 correction for dispersion interactions, along with the Goedecker–Teter–Hutter (GTH) TZVPP[59] basis set and pseudopotential. The optimized structure of quercetin was placed in proximity to the (100), (101), and (011) surfaces and the combined system was fully optimized. To study the interaction between quercetin and the BSA–$MnFe_2O_4$(101) complex, fragmental DFT calculations were performed using the CP2K code. The initial configuration for the DFT calculations was obtained from the molecular docking results, specifically the most stable structure where the (011) facet of the $MnFe_2O_4$ nanoparticle was bound to BSA, and quercetin was accommodated within the complex. All residues with a separation threshold of 5 Å were included. Tight convergence criteria (10^{-7} a.u.) were set for the SCF energy during the optimization process. The basis set superposition error (BSSE)[60] was applied to all calculations to correct the binding energy.

The binding energy (ΔE) of quercetin on the $MnFe_2O_4$ surface was calculated using the following equation:

$$\Delta E = E_{(complex)} - [E_{(MnFe_2O_4)} + E_{(quercetin)}],$$

where $E_{(complex)}$ is the total energy of the quercetin–$MnFe_2O_4$ system, $E_{(MnFe_2O_4)}$ is the energy of the isolated $MnFe_2O_4$ surface, and $E_{(quercetin)}$ is the energy of the isolated quercetin molecule. A negative value of ΔE indicates a favorable binding interaction.

2.2.3. Reduced density gradient (RDG). To further analyze the nature of the interactions between quercetin and the $MnFe_2O_4$ facets and in the complex with BSA, we performed reduced density gradient (RDG) analysis using the NCIplot program.[61] RDG is a dimensionless quantity that is sensitive to non-covalent interactions. We generated RDG isosurfaces and plotted the sign(λ_2)ρ function to characterize these interactions. The sign(λ_2) term helps to distinguish between attractive ($\lambda_2 < 0$) and repulsive ($\lambda_2 > 0$) interactions. We generated Reduced Density Gradient (RDG) isosurfaces and plotted the sign(λ_2)ρ function to characterize these interactions. The sign(λ_2) term helps to distinguish between attractive ($\lambda_2 < 0$) and repulsive ($\lambda_2 > 0$) interactions.

2.3. Statistical analysis

All of the quantitative data were expressed as mean with standard deviation (mean ± SD) unless otherwise stated. Statistical analysis was performed using GraphPad Prism software (GraphPad Prism 8).

3. Results and discussion

3.1. Experimental results

3.1.1. FTIR analysis of $MnFe_2O_4$@BSA and $MnFe_2O_4$@BSA–quercetin. In the FTIR spectrum of $MnFe_2O_4$@BSA nanoparticles, as shown in Fig. 2, a broad band observed at 3434 cm^{-1} is indicative of N–H stretching vibrations. Furthermore, a peak identified at 1570 cm^{-1} corresponds to H–O–H bending vibrations. The peaks at 523 cm^{-1} and 635 cm^{-1} are attributed to Fe–O stretching vibrations, providing evidence for the successful synthesis of the nanoparticles. In the analysis of the BSA component, the FTIR spectrum reveals a broad band at 3433 cm^{-1}, which is also associated with N–H stretching vibrations. Additional peaks at 2924, 1578, 1431, 1015, 808, and 648 cm^{-1} correspond to C–H stretching, asymmetric and symmetric COO^- stretching, C–O stretching, and vibrations related to the carbon skeleton, respectively. Overall, the results obtained from the FTIR analysis support the conclusion that the synthesis of $MnFe_2O_4$@BSA nanoparticles has been successfully achieved. The FTIR spectrum of $MnFe_2O_4$@BSA–quercetin nanoparticles is shown in Fig. 3.

3.1.2 TEM analysis. Fig. 4 illustrates that the TEM imaging revealed the nanoparticles to possess a spherical morphology, with an average diameter of around 7 nanometers.

3.1.3. XRD analysis. The XRD pattern obtained for the synthesized $MnFe_2O_4$ nanoparticles is presented here. The results indicate that the observed XRD pattern aligns with the standard XRD pattern for $MnFe_2O_4$, which is shown in Fig. 5.

3.1.4. Determining the size and zeta potential of nanoparticles. The results obtained from the DLS device for each of the formulations are shown in Fig. 6. Based on the results, the average hydrodynamic diameter of the BSA–$MnFe_2O_4$ nanoparticles is 85.27 ± 0.26 nm with a PDI of 0.25 (Fig. 6(A)), and the size of BSA–$MnFe_2O_4$–quercetin nanoparticles is 98.13 ± 0.78 nm with a PDI of 0.364 (Fig. 6(B)); the zeta potential of BSA–$MnFe_2O_4$ nanoparticles is −16 mV (Fig. 6(C)) and the zeta potential of BSA–$MnFe_2O_4$–quercetin nanoparticles is −13.8 mV (Fig. 6(D)). The zeta potential of nanoparticles plays a crucial role in determining their colloidal stability. Zeta potential is a measure of the electrical charge on the surface of nanoparticles, which affects their interparticle interactions. A high positive or negative zeta potential (typically $> \pm 30$ mV) leads to strong electrostatic repulsion between particles, preventing aggregation and enhancing colloidal stability.[62] This ensures the nanoparticles remain dispersed in the solution and do not clump together. If the zeta potential is low (close to 0 mV), the electrostatic repulsion is weak, allowing van der Waals forces to dominate, which increases the likelihood of aggregation and instability.[63] Thus, maintaining an optimal zeta potential is key to ensuring long-term dispersion and stability of nanoparticles in solution, which is

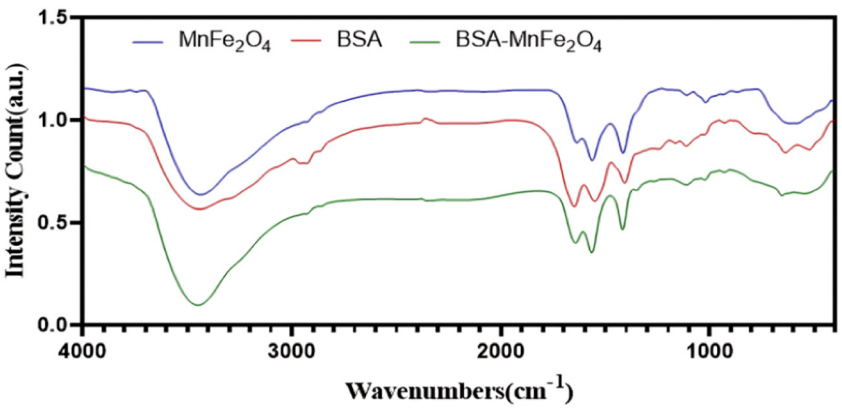

Fig. 2 FT-IR analysis of synthesized $MnFe_2O_4$–BSA nanoparticles.

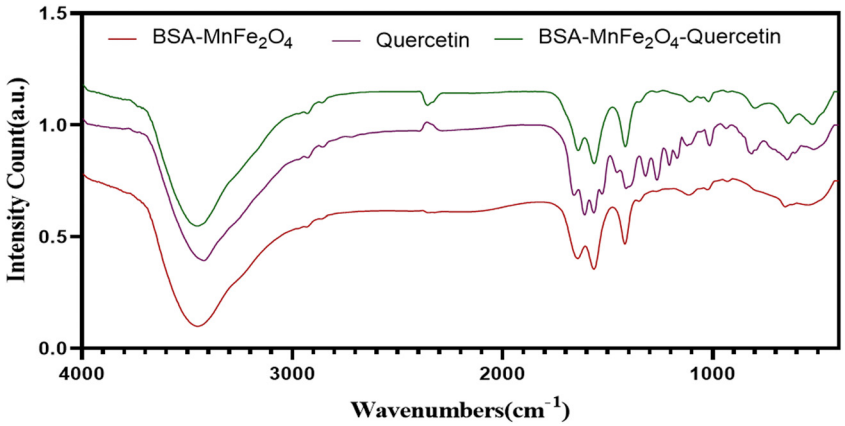

Fig. 3 FT-IR analysis of synthesized $MnFe_2O_4$–BSA–quercetin nanoparticles.

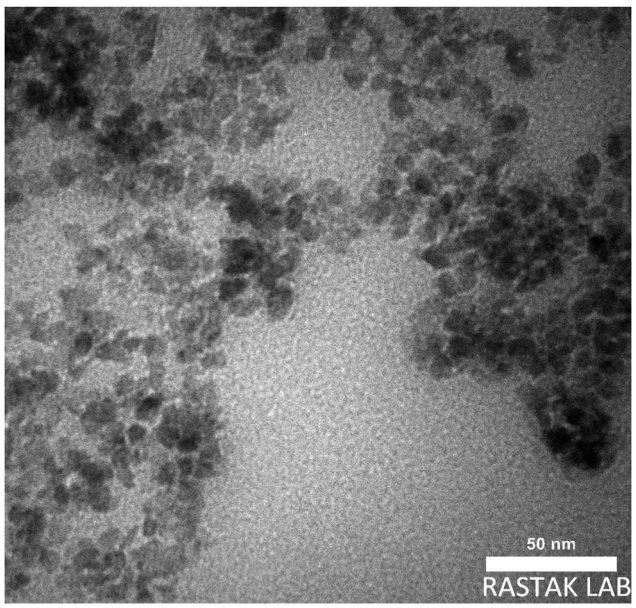

Fig. 4 TEM imaging of synthesized nanoparticles.

important for their effective applications in various fields, including drug delivery and imaging.

3.1.5. UV-vis analysis. The UV-vis spectrum of the synthesized nanoparticles is presented in Fig. 7. The spectrum corresponding to BSA reveals distinct peaks at 260 nm and 240 nm, which are indicative of BSA nanoparticles and provide evidence for their successful synthesis. Furthermore, the spectrum of $MnFe_2O_4$–BSA nanoparticles also shows a peak near 260 nm, thereby corroborating the successful fabrication of these nanoparticles.

3.1.6. Drug loading. The drug loading capacity of quercetin in the nanoparticles was measured using a UV-vis spectrophotometer. The analysis showed that the drug loading efficiency was 27.5%.

3.1.7. Drug release behavior. The release kinetics of quercetin from nanoparticles were evaluated under both neutral and acidic pH conditions. The drug release profiles, illustrated in Fig. 8, indicate a progressive release of the free drug over time. Quercetin was investigated in two distinct phosphate-buffered saline (PBS) solutions with pH levels of 7.4 (physiological pH of blood and healthy tissue) and 5.7 (intracellular pH of cancer cells), as shown in Fig. 8. Notably, the peak release from the nanoparticle system occurred at 120 h in both media. In the neutral environment, approximately 41% of the quercetin was released after 120 h, while a markedly higher release of 62% was recorded in the acidic environment. These results suggest that quercetin is released more effectively under acidic conditions. This section of our study aims to assess the performance of the drug release system across two critical pH extremes: physiological conditions (pH 7.4)[64] and a notably

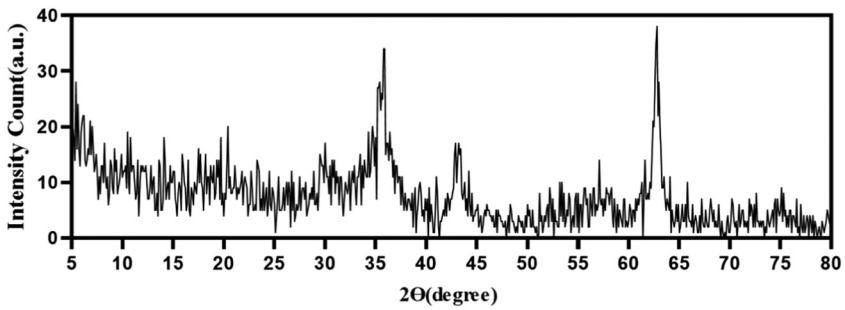

Fig. 5 XRD analysis of synthesized nanoparticles.

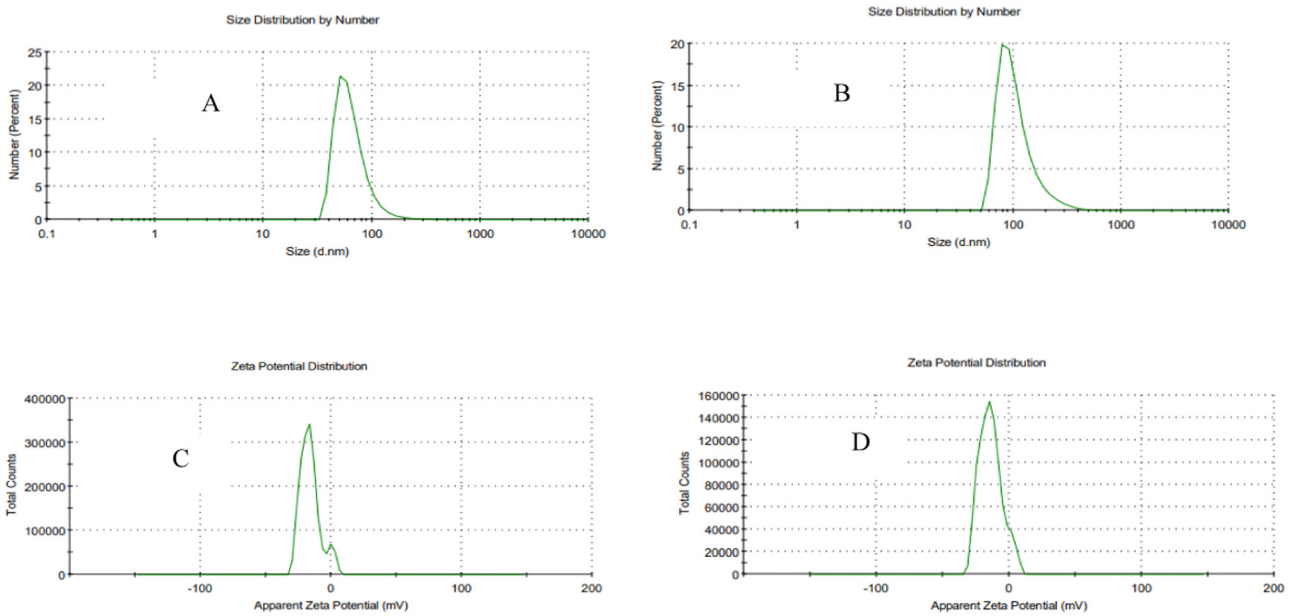

Fig. 6 DLS analysis related to the size of nanoparticles. (A). DLS of BSA–$MnFe_2O_4$ nanoparticles. (B) DLS of BSA@$MnFe_2O_4$–quercetin nanoparticles. (C) Zeta potential of BSA–$MnFe_2O_4$ nanoparticles. (D) Zeta potential of BSA@$MnFe_2O_4$–quercetin nanoparticles.

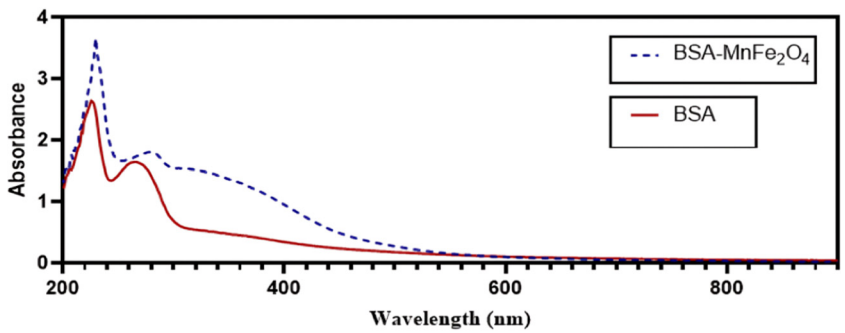

Fig. 7 The UV-vis spectra of the synthesized nanoparticles are illustrated. The blue curve corresponds to BSA–$MnFe_2O_4$ nanoparticles and the red curve indicates the absorbance of BSA.

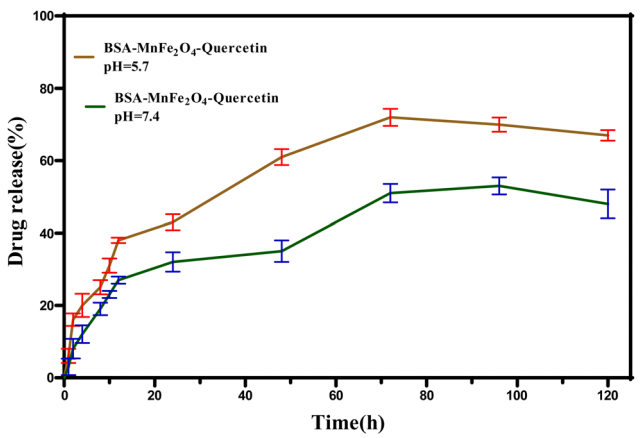

Fig. 8 Quercetin release profile.

acidic environment (pH 5.7). The pH of 7.4 is utilized as a reference point for evaluating the stability of the system within the bloodstream and healthy tissues, where it helps minimize the risk of premature drug release. Conversely, the acidic pH of 4.4–6 is selected to replicate the stringent acidic conditions that occur within intracellular compartments[31] following cellular uptake. By evidencing a significant pH-dependent release mechanism between these two clearly defined conditions, our research underscores the system's potential for targeted drug delivery and intracellular activation objectives of our investigation. Exploring these critical physiological parameters provides compelling initial evidence of the system's sensitivity to relevant pH gradients. Recent *in vitro* research indicates that quercetin can be released in a sustained manner under acidic conditions. This finding points to improved drug retention and intracellular delivery within the tumor microenvironment. The controlled release mechanism is anticipated to reduce systemic toxicity by restricting drug release at physiological pH (7.4). When paired with magnetic targeting, this pH-responsive release method is expected to enhance drug localization and extend therapeutic exposure at tumor sites *in vitro*. However,

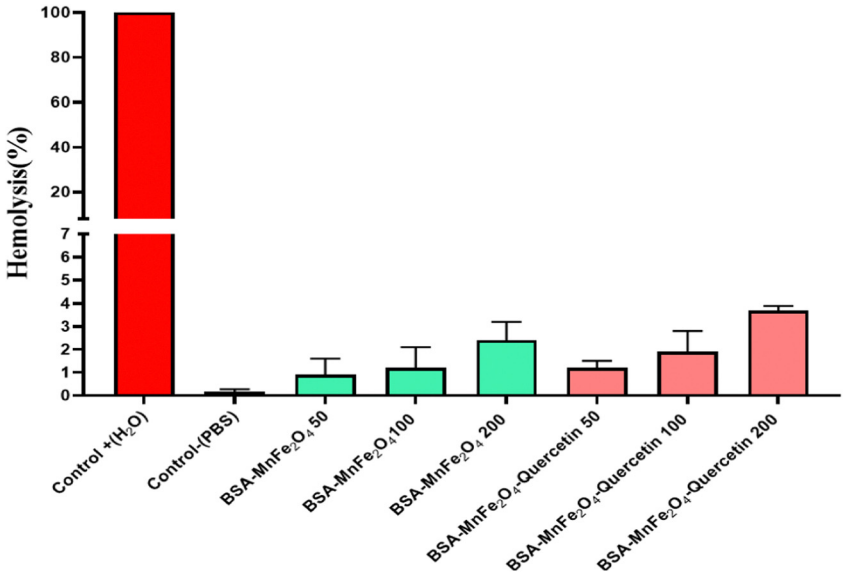

Fig. 9 The hemolysis assay to evaluate the biocompatibility of the prepared nanoparticles.

the intricate nature of the *in vivo* environment, which includes variables such as blood flow and drug clearance, highlights the need for further studies to validate these findings and evaluate the actual therapeutic effectiveness and safety.

3.1.8. Hemolysis assay. The hemolysis assay was conducted to evaluate the biocompatibility of the nanoparticles. In this test, water was used as a positive control and phosphate-buffered saline (PBS) was used as a negative control. The results of the hemolysis assay are presented in Fig. 9. Various concentrations of nanoparticles were prepared and subsequently assessed. The findings indicate that the nanoparticles exhibited a dose-dependent hemolytic effect. Due to the direct interaction of the drug with blood tissue, it is essential to evaluate the hematotoxicity. Consequently, the hematotoxicity biocompatibility study of BSA@$MnFe_2O_4$ and BSA@$MnFe_2O_4$–quercetin nanosystems was performed. Various concentrations of nanoparticles were investigated, and the data from this study indicated dose-dependent toxicity of nanoparticles. Moreover, according to observations, nanoparticles are safe up to a concentration of 200 μg mL^{-1} and display less than 5% toxicity.

3.1.9. Therapeutic impacts on cancerous cells. The therapeutic efficacy of chemotherapy and radiotherapy in combination with nanoparticle-loaded quercetin was assessed using the MTT assay on 4T1 tumor cells under both standard conditions and conditions involving nanoparticle treatment. The $MnFe_2O_4$–BSA–quercetin formulation demonstrated a dose-dependent cytotoxic effect. As illustrated in Fig. 10, the drug-loaded nanoparticles resulted in reduced cell viability at the administered concentrations (20, 60, and 80 μg mL^{-1}) relative to the free drug. This observed reduction in viability may be attributed to enhanced drug absorption by tumor cells and the synergistic interactions facilitated by the nanoparticle carrier. Moreover, when subjected to 4 Gy radiation, the catalytic capacity of $MnFe_2O_4$–BSA–quercetin nanoparticles for the generation of ROS was significantly augmented, resulting in a further decline in cell viability at the tested concentrations when compared to the non-irradiated samples.

3.1.10. LD_{50} as an *in vivo* biosafety indicator. To confirm the *in vivo* biosafety of developed $MnFe_2O_4$@BSA–quercetin and accordingly increase the overall chances of these nanoparticles

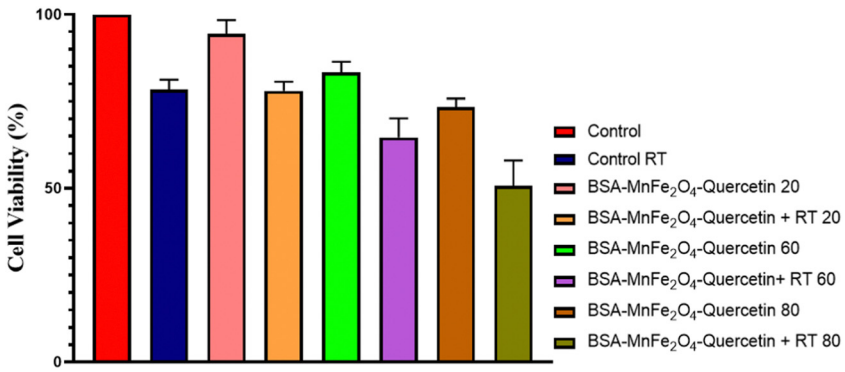

Fig. 10 The MTT assay on 4T1 tumor cells.

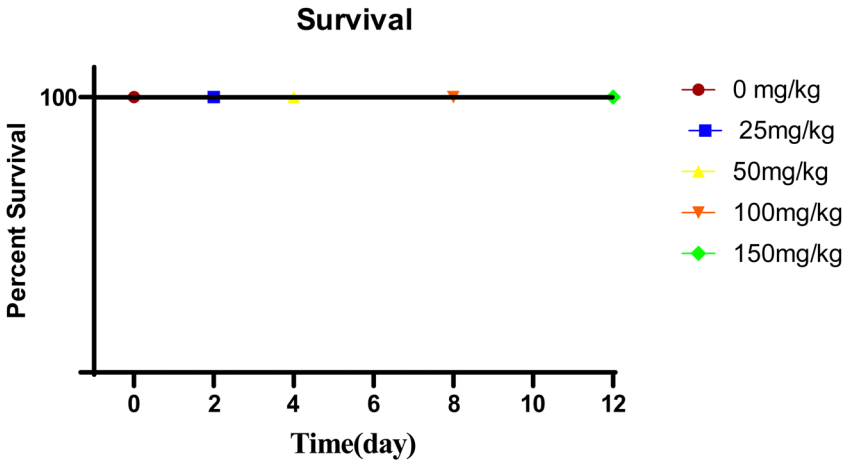

Fig. 11 LD_{50} assay.

to reach the preclinical studies, *in vivo* biosafety was primarily assessed using LD_{50} assay. Mice received various concentrations of $MnFe_2O_4$@BSA–quercetin nanoparticles (0, 25, 50, 100 and 150 mg kg^{-1}) by intravenous injection, and their survival rate and behavior were fully monitored. As depicted in Fig. 11, a Cox Regression diagram was used to represent the obtained results. Interestingly, after injection of $MnFe_2O_4$@BSA–quercetin, all mice survived and no deaths were observed in the treated groups, as well as monitoring of body weight revealed no significant changes relative to the control group. Furthermore, no significant side effects could be observed in the blood panel count biochemical analysis after injection of $MnFe_2O_4$@BSA–quercetin. These outcomes disclosed the fact that $MnFe_2O_4$@BSA–quercetin nanoparticles had no toxic effects and provided further evidence for *in vivo* biosafety of $MnFe_2O_4$@BSA–quercetin nanoparticles for (pre)clinical exploration.

3.2. Computational results

3.2.1. Molecular docking results. The molecular docking simulation revealed that quercetin was accommodated within a binding pocket located in the Subdomain IIA of BSA (Fig. 12). Subdomain IIA is one of the two primary drug-binding sites in BSA (the other being Subdomain IIIA). Many small molecules, including flavonoids like quercetin, are known to bind preferentially in this region. For example, Shaghaghi *et al.*[65] demonstrated that quercetin binds to the Subdomain IIA of BSA, with molecular docking revealing favorable interactions and electrostatic forces as the primary binding mechanism. This subdomain is known for its relatively hydrophobic character, which is consistent with the binding of aromatic and polycyclic ligands. The docked pose, selected based on the lowest binding energy (−5.17 kcal mol^{-1}), shows that quercetin primarily interacts with amino acid residues within this subdomain of BSA, through both polar and non-polar interactions. Another study conducted by Mohammadi *et al.*[66] involving quercetin's interaction with proteins reported binding energies in the range of −5.95 kcal mol^{-1} for other targets, suggesting similar magnitudes for BSA interactions. As shown in Fig. 12, the hydroxyl

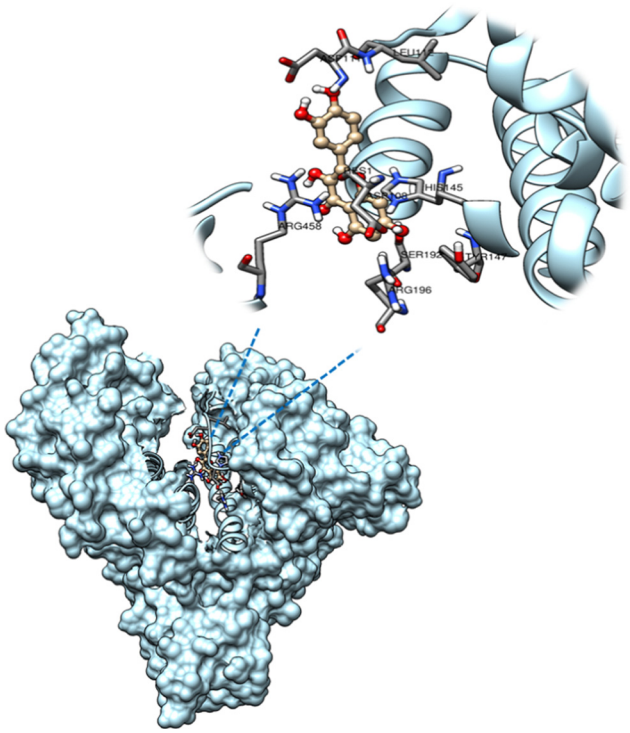

Fig. 12 Molecular docking results of quercetin (wheat, sticks) in BSA (light blue, cartoon). Key interacting amino acid residues are labeled (for clarity, only the chain A is shown).

groups of quercetin form specific interactions, including potential hydrogen bonds and van der Waals forces, with the side chains of ASP192, HIS145, SER194, ARG196, and ARG458, which are all located within or close to the Subdomain IIA of BSA.

Molecular docking simulations revealed distinct binding patterns for the different $MnFe_2O_4$ facets within BSA, with each exhibiting favorable interaction energies. Fig. 13 illustrates the molecular docking poses of the $MnFe_2O_4$ nanoparticles inside the BSA structure. The (011) facet was primarily accommodated

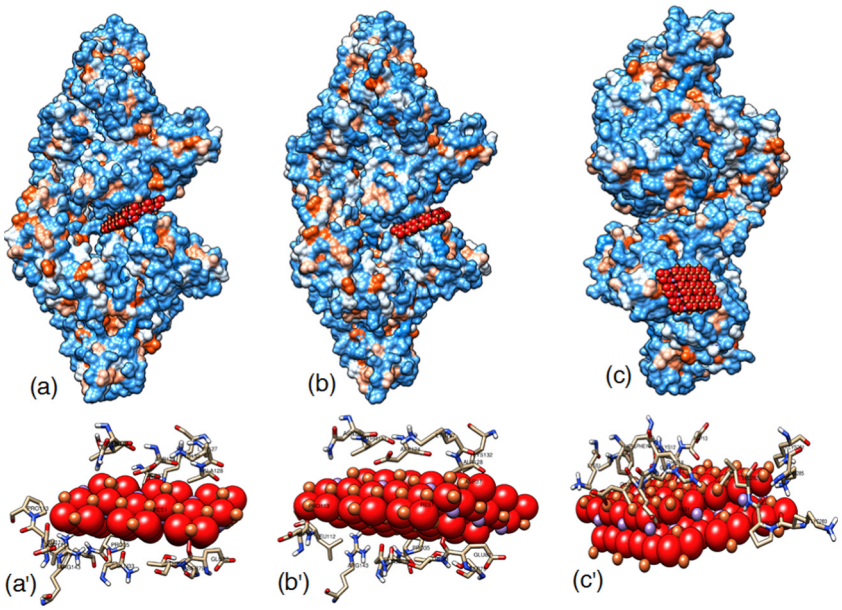

Fig. 13 Molecular docking poses of the $MnFe_2O_4$ nanoparticles [(a) (011) facet, (b) (101) facet, and (c) (100) facet] bound to bovine serum albumin (BSA). Top panels display the overall binding configuration of each facet within BSA (surface representation), while bottom panels [(a′), (b′), and (c′)] show a detailed view of the interactions between the $MnFe_2O_4$ facets (red/copper spheres and van der Waals representation) and key amino acid residues of BSA (tan, sticks).

at the Subdomain IB–IIB interface region of BSA, interacting with amino acid residues such as ARG124, LYS127, ALA128, ASP37, GLU80, SER79, PRO113, GLU112, and ARG143 (Fig. 13(a)). The (101) facet showed a different binding mode, located in a region spanning Subdomains IA and IB, interacting with residues including ASP127, LYS132, LYS41, GLU33, LYS31, SER110, and ARG48 (Fig. 13(b)). In contrast, the (100) facet is bound to an extended surface region involving different subdomains and interacting with residues such as ASP12, LYS13, GLU117, PHE14, LYS51, GLU53, ASP282, and PRO280 (Fig. 13(c)). The binding affinity varied among the facets: the (101) facet exhibited the highest binding affinity with an estimated binding energy of -9.21 kcal mol^{-1} and an inhibition constant of 178.74 nM. The (011) facet exhibited a binding energy of -7.75 kcal mol^{-1} and a K_i of 2.09 μM, while the (100) facet had a binding energy of -7.23 kcal mol^{-1} and a K_i of 5.04 μM. Energetic analysis revealed that the van der Waals and hydrogen bond desolvation energy terms predominantly contributed to the favorable binding in all three facets, with a negligible electrostatic contribution in all cases. A comparison of the DFT derived binding energies and the docking results showed a similar trend, thus supporting the findings.

The molecular docking simulation revealed that quercetin was accommodated within the BSA–$MnFe_2O_4$ (101) complex (Fig. 14). In this new environment, the docked pose, selected based on the lowest binding energy (-7.19 kcal mol^{-1}), shows that quercetin interacts primarily with amino acid residues of BSA as well as with the (101) facet of $MnFe_2O_4$. As shown in Fig. 14, quercetin interacts with the side chains of various amino acids of BSA, for example, ASP129, LYS132, GLU125,

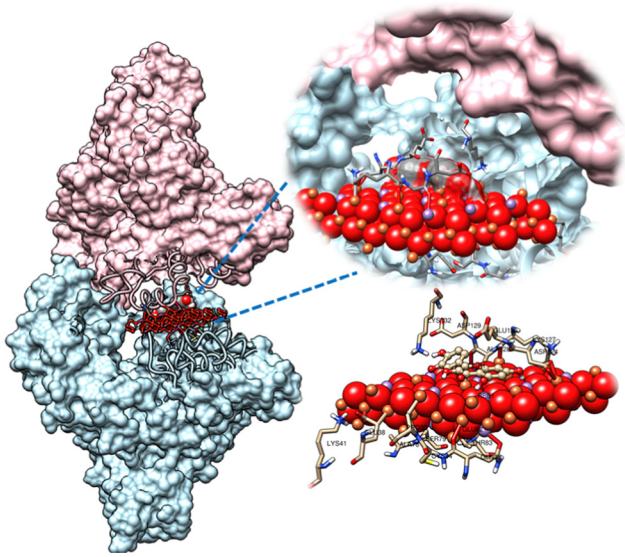

Fig. 14 Molecular docking results of quercetin (grey spheres) in the BSA–$MnFe_2O_4$ (101) complex. The BSA protein surface in light blue (chain A) at the bottom and pink (chain B) at the top. The (101) facet (red/copper spheres, van der Waals representation) and key interacting amino acid residues are labeled.

LYS127, SER79, ALA78, GLU76, and HIS83, through hydrogen bonds and van der Waals interactions.

Table 1 summarizes the binding energies and related data for all the studied systems. The $MnFe_2O_4$ facets had smaller ligand efficiencies (0.05 for the (011) facet and 0.06 for the (101) facet) than quercetin. This is mainly because the LE is lower in the nanoparticles, which also suggests that the interactions are

Table 1 Molecular docking results for $MnFe_2O_4$ facets and quercetin with BSA and complexes

System	Binding energy (kcal mol^{-1})	Ligand efficiency	Inhibition constant (K_i)	K_i units
$MnFe_2O_4$(011)–BSA	−7.75	0.05	2.09	μM
$MnFe_2O_4$(101)–BSA	−9.21	0.06	178.74	nM
$MnFe_2O_4$(100)–BSA	−7.23	−0.05	5.04	μM
Quercetin–BSA	−5.17	−0.23	160.97	μM
Quercetin–BSA–$MnFe_2O_4$ (101)	−7.19	−0.33	5.37	μM

less specific. On the other hand, quercetin had a larger binding affinity towards BSA alone than in the presence of $MnFe_2O_4$. This suggests that there is competition for the binding site. The inhibition constant (K_i) values, which reflect the affinity of the various complexes and facets for BSA, further support the differences observed in binding energies. The $MnFe_2O_4$ (101) facet showed the lowest K_i value at 178.74 nM, compared with the (011) and (100) facets, which showed K_i values at 2.09 μM and 5.04 μM respectively. In addition to all facets having distinct affinity, the (101) also disrupts the quercetin binding within the system, thus providing an advantage for the nanoparticle in the system.

3.2.2. Density functional theory (DFT) results. Density functional theory (DFT) calculations were performed on docked configurations of quercetin adsorbed onto various facets of $MnFe_2O_4$ nanoparticles. Fig. 15 shows the most stable geometry optimization of quercetin with different facets of $MnFe_2O_4$. The optimized geometries revealed that quercetin binds to the nanoparticle surfaces *via* coordination between its oxygen-containing functional groups (–OH and –C═O) and the metal sites (Mn and Fe). For instance, on the (100) facet, key bond distances of 1.908, 2.116, and 2.501 Å were observed, yielding a binding energy of approximately −59.61 kcal mol^{-1}. Similarly, the (101) facet exhibited even stronger binding (up to ∼−67.14 kcal mol^{-1}), while the (011) facet showed a moderately strong interaction with a binding energy of −58.31 kcal mol^{-1}. These values indicate that the adsorption is predominantly chemisorptive in nature, driven by strong metal–ligand interactions. Importantly, for the $MnFe_2O_4$@BSA–quercetin (101) complex, the binding energy was found to be −77.2 kcal mol^{-1}, indicating a significantly more stable and favorable interaction within this specific ternary system. The measured distances between specific atoms are as follows: the OH group on the (101) facet of the protein shows a separation of 1.696 Å. Additionally, this group interacts with another region of the molecule within the protein at distances of 2.638 Å and 1.383 Å. From these results, we confirmed the creation of three hydrogen bonds in different compounds; however, in the compound "quercetin–BSA–$MnFe_2O_4$", it was shown that there exist

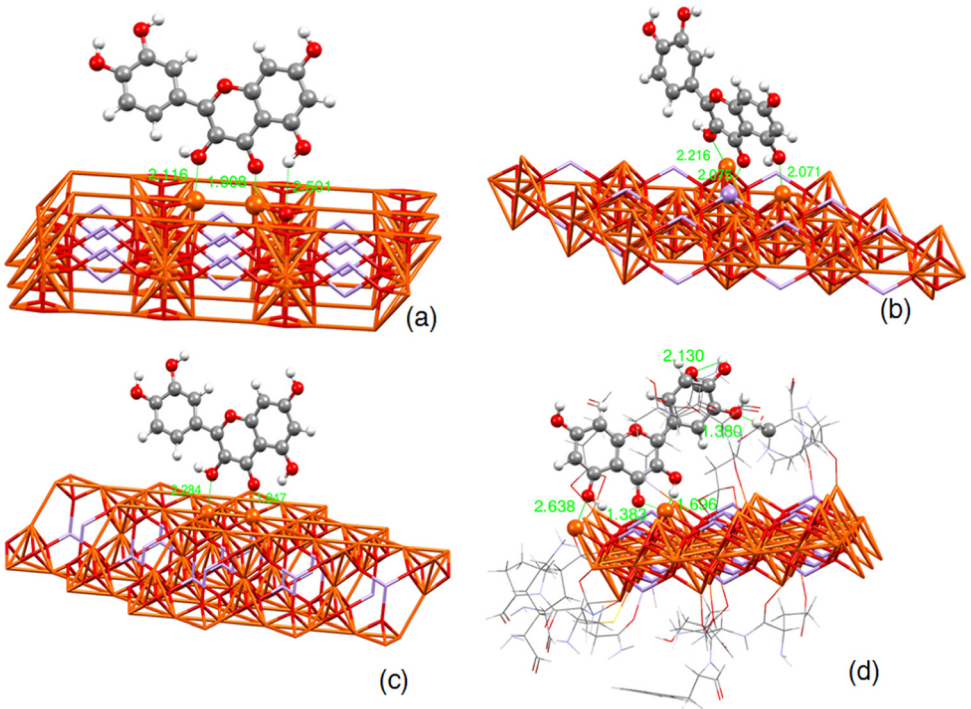

Fig. 15 DFT-optimized structures illustrating the interactions of quercetin with different $MnFe_2O_4$ facets and the BSA complex. (a) shows the interaction of quercetin with the (100) facet, (b) with the (101) facet, (c) with the (011) facet, and (d) the interaction within the $MnFe_2O_4$@BSA–quercetin (101) complex. Distances between quercetin and the material surfaces are labeled in Å. Ice blue, orange, red, gray, and white represent Mn, Fe, O, C, and H, respectively.

Table 2 DFT-calculated interaction energies for interatomic interactions between quercetin and $MnFe_2O_4$ (011), (100), and (101) facets and the (101) system in the complex

System	Interaction energy (kcal mol^{-1})
Quercetin–$MnFe_2O_4$ (011)	−58.31
Quercetin–$MnFe_2O_4$ (100)	−59.61
Quercetin–$MnFe_2O_4$ (101)	−67.14
Quercetin–BSA–$MnFe_2O_4$ (101)	−77.2

even more binding points and hydrogen bond creation that stabilize the complex and can create other interactions to promote the system. The related interaction energies are provided in Table 2.

3.2.3. Reduced density gradient (RDG) analysis. To comprehensively understand the adsorption behavior of quercetin on $MnFe_2O_4$ nanoparticles, we performed RDG analysis on three distinct facets – (011), (101), and (100) – and further examined the influence of BSA on the interaction with the (101) facet. The resulting RDG plots and isosurfaces provide insights into the interplay of van der Waals forces, hydrogen bonding/coordination, and steric effects across these systems. The results of RDG analysis are provided in Fig. 16. The analysis revealed that the facet structure significantly dictates the nature of the quercetin–$MnFe_2O_4$ interaction. On the (011) facet, the RDG plots indicated a balanced contribution from strong, localized hydrogen bonding/coordination interactions with surface oxygen and Mn atoms and weaker van der Waals forces. Conversely, the (101) facet showed a dominance of van der Waals interactions, with more restricted hydrogen bonding and potential steric limitations imposed by the surface structure. The (100) facet exhibited an intermediate profile, where van der Waals forces remained significant, but with a shifted balance, potentially leading to fewer interactions with Mn. This is correlated to steric hindrance as shown on RDG plots by red areas. The inclusion of BSA profoundly alters the interaction landscape. On the $MnFe_2O_4$@BSA (101) complex, the RDG analysis revealed a significant increase in van der Waals forces, largely attributed to the presence of BSA residues. This shift is accompanied by a decrease in direct hydrogen bonding/coordination between quercetin and the $MnFe_2O_4$ surface, suggesting that BSA sterically hinders access to surface binding sites and competes for interactions with quercetin through the interaction with BSA residues. The prominence of red zones in the RDG plot supports this.

Quercetin's electrostatic potential (ESP) distribution was analyzed to understand its interaction with $MnFe_2O_4$. Fig. 17 presents the ESP-mapped molecular surface, highlighting the electron density distribution and potential interaction sites. The analysis revealed distinct regions of positive and negative ESP, with negative ESP regions (red zones) around oxygen atoms in hydroxyl and carbonyl functional groups and positive ESP regions (blue zones) corresponding to electropositive hydrogen atoms within hydroxyl groups. Neutral regions (green/yellow zones) were less reactive, mainly covering aromatic rings, potentially contributing to π–π stacking interactions with the surface. The study investigated quercetin's interaction with $MnFe_2O_4$ on three different facets (011), (101), and (100), and

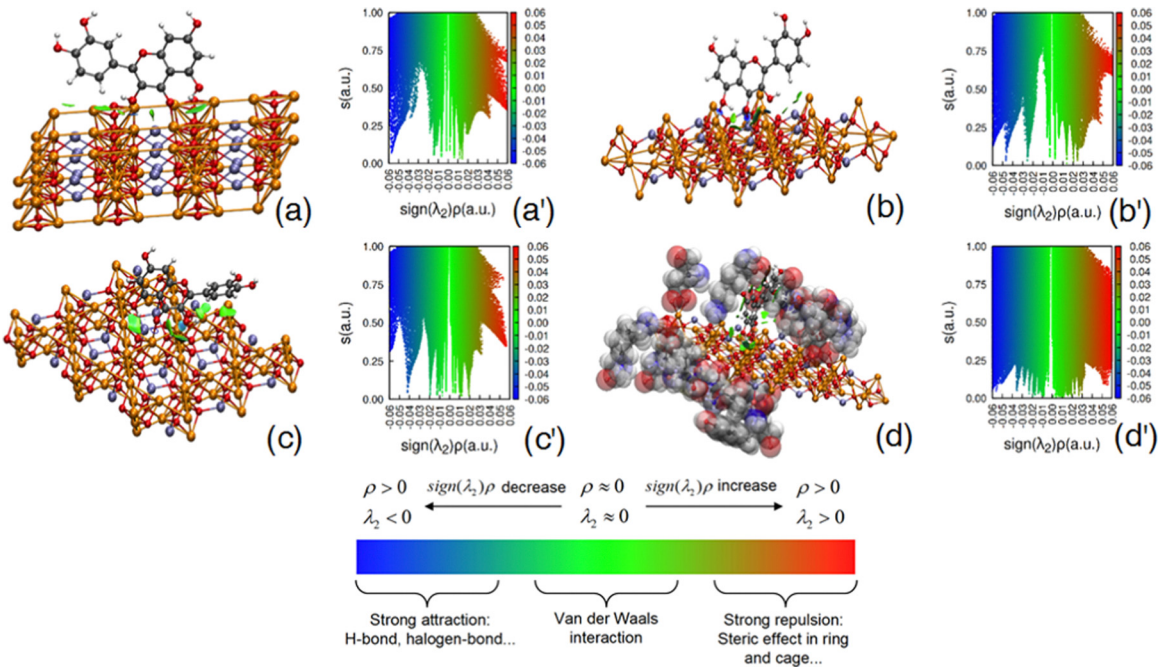

Fig. 16 Reduced density gradient scatter plots and the corresponding molecular models illustrating the adsorption of quercetin on $MnFe_2O_4$ (011) [(a) and (a′)], (101) [(b) and (b′)], and (100) [(c) and (c′)] facets, as well as on the BSA–$MnFe_2O_4$ (101) complex [(d) and (d′)]. The color code in the RDG plots signifies the strength and nature of interactions: blue (strong attraction), green (van der Waals), and red (steric repulsion). Ice blue, orange, red, gray, and white represent Mn, Fe, O, C, and H, respectively.

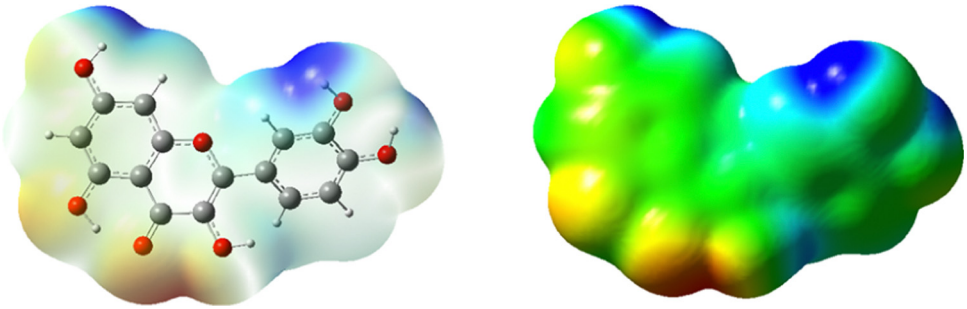

Fig. 17 Electrostatic potential (ESP) maps of quercetin in transparent (left) and solid (right) forms. The maps depict electron-rich (red) and electron-deficient (blue) regions, indicating potential interaction sites.

its binding with BSA-functionalized $MnFe_2O_4$ (101). The reduced density gradient (RDG) analysis revealed that the carbonyl and hydroxyl groups of quercetin strongly interact with surface Mn and Fe metals through electrostatic coordination. The hydroxyl groups may also form hydrogen bonds with surface oxygens, enhancing binding stability. The (101) facet, with a different charge distribution, binds through charge-assisted interactions, with electronegative oxygen atoms coordinating with surface metal cations and hydroxyl groups contributing to hydrogen bonding. The study investigated quercetin's interaction with $MnFe_2O_4$ on three different facets (011), (101), and (100), and its binding with BSA-functionalized $MnFe_2O_4$ (101). The Reduced Density Gradient (RDG) analysis revealed that the carbonyl and hydroxyl groups of quercetin strongly interact with surface Mn and Fe metals through electrostatic coordination. The hydroxyl groups may also form hydrogen bonds with surface oxygens, enhancing binding stability. The (101) facet, with a different charge distribution, binds through charge-assisted interactions, with electronegative oxygen atoms coordinating with surface metal cations and hydroxyl groups contributing to hydrogen bonding. The $MnFe_2O_4$ (100) facet of $MnFe_2O_4$ has unique interaction sites that influence quercetin binding. Quercetin primarily interacts *via* metal coordination, forming strong bonds with available cations. The planar aromatic rings may engage in π–π stacking interactions with the surface, stabilizing adsorption. The RDG analysis confirms moderate non-covalent interactions. When conjugated with bovine serum albumin (BSA), the interaction pattern shifts due to polar amino acid residues. New hydrogen bonding interactions between quercetin's hydroxyl/carbonyl groups and BSA's polar functional groups are highlighted. BSA-functionalization enhances quercetin binding by introducing additional non-covalent interactions.

4. Conclusion

This study provides a comprehensive and integrative investigation of BSA-coated $MnFe_2O_4$ nanoparticles as a promising quercetin drug delivery platform, combining detailed computational modeling with robust experimental validation. Our findings demonstrate significant interactions between quercetin, the $MnFe_2O_4$ nanoparticle surface (emphasizing the importance of Mn coordination sites), and BSA, with computational binding energies (−67.14 kcal mol^{-1} for the (101) facet) aligning strongly with the observed experimental drug loading capacity of 27.5%. Critically, Reduced Density Gradient (RDG) analysis revealed the facet-dependent nature of quercetin adsorption, demonstrating how the interplay of hydrogen bonding and van der Waals forces varies across the (011), (101), and (100) facets, influencing quercetin stability and release. The enhanced quercetin release (62% at pH 5.7) confirms the pH-responsive nature of the system, a crucial feature for targeted drug delivery to the acidic tumor microenvironment.

The novelty of our approach lies in the synergistic combination of the BSA coating and facet-specific computational analysis, offering a refined understanding of quercetin–nanoparticle interactions. This approach demonstrates that the BSA coating modifies the adsorption landscape and enhances drug binding, leading to reduced hemolytic activity. The simulations also show the promise of combining BSA and $MnFe_2O_4$ (101) in improving binding energy. The predicted binding is consistent with the observed reduction in cell viability (45% at 200 μg mL^{-1}), suggesting the anticancer activity of the drug delivery system. These findings underscore the importance of considering surface crystallography in the design of effective nano-based drug delivery systems. Future research should focus on synthesizing nanoparticles with controlled facet exposure to further optimize quercetin loading and release. Further studies are needed to evaluate the drug release rate in a more *in vitro* environment and test the anticancer efficacy of this system *in vivo*, particularly in combination with external stimuli such as alternating magnetic fields to enhance thermal energy and promote targeted hyperthermia. These investigations will ultimately pave the way for the development of advanced, biocompatible, and targeted drug delivery strategies for cancer therapy, maximizing therapeutic benefits while minimizing off-target effects.

Data availability

The datasets used during the current study are available from the corresponding author upon reasonable request.

Conflicts of interest

There are no conflicts of interest to declare.

Acknowledgements

We gratefully acknowledge the Iran National Science Foundation (INSF) under project No-4023992 and the Deputy of Research at Zanjan University of Medical Sciences [A-12-430-79, ethical code: IR. ZUMS. BLC.1403.012] for their invaluable institutional support.

References

1 X. Kong, P. Gao, J. Wang, Y. Fang and K. C. Hwang, Advances of medical nanorobots for future cancer treatments, *J. Hematol. Oncol.*, 2023, **16**(1), 74.
2 A. Mohammadi, N. Hashemi, Z. Asghariha, M. S. Hosseini and H. Danafar, SWCNTs functionalized with gold nanoradiosensitizers as radiosensitizers for enhanced radiotherapy in breast cancer, *Results Chem.*, 2025, **14**, 102113.
3 J. Wang and S.-G. Wu, Breast cancer: an overview of current therapeutic strategies, challenge, and perspectives, *Breast Cancer: Targets Ther.*, 2023, 721–730.
4 J. A. Burket, W. R. Cannon, L. F. Jacome and S. I. Deutsch, MK-801, a noncompetitive NMDA receptor antagonist, elicits circling behavior in the genetically inbred Balb/c mouse strain, *Brain Res. Bull.*, 2010, **83**(6), 337–339.
5 X. Meng, X. Zhang, M. Liu, B. Cai, N. He and Z. Wang, Fenton reaction-based nanomedicine in cancer chemodynamic and synergistic therapy, *Appl. Mater. Today*, 2020, **21**, 100864.
6 P. Sharma, A. B. Jha, R. S. Dubey and M. Pessarakli, Reactive oxygen species, oxidative damage, and antioxidative defense mechanism in plants under stressful conditions, *J. Bot.*, 2012, **2012**(1), 217037.
7 M. Deniz, E. Sezer, A. Tetik and S. Ulukaya, Evaluation of the Brain Cellular Damage during Liver Transplantations, *Niger. J. Clin. Pract.*, 2023, **26**(8), 1063–1068.
8 R. Topkaya, H. Güngüneş, Ş. Eryiğit, S. E. Shirsath, A. Yıldız and A. Baykal, Effect of bimetallic (Ni and Co) substitution on magnetic properties of $MnFe_2O_4$ nanoparticles, *Ceram. Int.*, 2016, **42**(12), 13773–13782.
9 H. Sies and D. P. Jones, Reactive oxygen species (ROS) as pleiotropic physiological signalling agents, *Nat. Rev. Mol. Cell Biol.*, 2020, **21**(7), 363–383.
10 Y. Gu, R. Piñol, R. Moreno-Loshuertos, C. D. Brites, J. Zeler, A. Martínez, G. Maurin-Pasturel, P. Fernández-Silva, J. Marco-Brualla and P. Téllez, Local temperature increments and induced cell death in intracellular magnetic hyperthermia, *ACS Nano*, 2023, **17**(7), 6822–6832.
11 J. Fang, H. Nakamura and H. Maeda, The EPR effect: Unique features of tumor blood vessels for drug delivery, factors involved, and limitations and augmentation of the effect, *Adv. Drug Delivery Rev.*, 2011, **63**(3), 136–151.
12 Y. Gu, R. Piñol, R. Moreno-Loshuertos, C. D. S. Brites, J. Zeler, A. Martínez, G. Maurin-Pasturel, P. Fernández-Silva, J. Marco-Brualla, P. Téllez, R. Cases, R. N. Belsué, D. Bonvin, L. D. Carlos and A. Millán, Local Temperature Increments and Induced Cell Death in Intracellular Magnetic Hyperthermia, *ACS Nano*, 2023, **17**(7), 6822–6832.
13 B. Karunanithi, K. Manimaran and M. Srividhya, Isolation and characterization of amentoflavone – BSA coated polymer nanoparticles using Cassia fistula leaf extract against antibacterial and anticancer activity, *Biomass Convers. Biorefin.*, 2024, **14**(14), 16319–16328.
14 M. Hasanuzzaman, M. Bhuyan, F. Zulfiqar, A. Raza, S. M. Mohsin, J. A. Mahmud, M. Fujita and V. Fotopoulos, Reactive Oxygen Species and Antioxidant Defense in Plants under Abiotic Stress: Revisiting the Crucial Role of a Universal Defense Regulator, *Antioxidants*, 2020, **9**(8), 681–733.
15 B. Karunanithi, K. Manimaran and M. Srividhya, Isolation and characterization of amentoflavone-BSA coated polymer nanoparticles using Cassia fistula leaf extract against antibacterial and anticancer activity, *Biomass Convers. Biorefin.*, 2024, **14**(14), 16319–16328.
16 J. K. Patra, G. Das, L. F. Fraceto, E. V. R. Campos, M. d P. Rodriguez-Torres, L. S. Acosta-Torres, L. A. Diaz-Torres, R. Grillo, M. K. Swamy, S. Sharma, S. Habtemariam and H.-S. Shin, Nano based drug delivery systems: recent developments and future prospects, *J. Nanobiotechnol.*, 2018, **16**, 71.
17 I. Salahshoori, Z. Ramezani, I. Cacciotti, A. Yazdanbakhsh, M. K. Hossain and M. Hassanzadeganroudsari, Cisplatin uptake and release assessment from hydrogel synthesized in acidic and neutral medium: An experimental and molecular dynamics simulation study, *J. Mol. Liq.*, 2021, **344**, 117890.
18 C. J. Rijcken, O. Soga, W. E. Hennink and C. F. van Nostrum, Triggered destabilisation of polymeric micelles and vesicles by changing polymers polarity: an attractive tool for drug delivery, *J. Controlled Release*, 2007, **120**(3), 131–148.
19 J. W. Park, K. Hong, D. B. Kirpotin, G. Colbern, R. Shalaby, J. Baselga, Y. Shao, U. B. Nielsen, J. D. Marks, D. Moore, D. Papahadjopoulos and C. C. Benz, Anti-HER2 immunoliposomes: enhanced efficacy attributable to targeted delivery, *Clin. Cancer Res.*, 2002, **8**(4), 1172–1181.
20 J. Daduang, A. Palasap, S. Daduang, P. Boonsiri, P. Suwannalert and T. Limpaiboon, Gallic acid enhancement of gold nanoparticle anticancer activity in cervical cancer cells, *Asian Pac. J. Cancer Prev.*, 2015, **16**(1), 169–174.
21 C. Samorì, H. Ali-Boucetta, R. Sainz, C. Guo, F. M. Toma, C. Fabbro, T. Da Ros, M. Prato, K. Kostarelos and A. Bianco, Enhanced anticancer activity of multi-walled carbon nanotube–methotrexate conjugates using cleavable linkers, *Chem. Commun.*, 2010, **46**(9), 1494–1496.
22 S. Naderlou, M. Vahedpour and D. M. Franz, Functionalization Strategy in 2D Flexible Zn(BTTB)-MOF for Improving Storage and Release of Anticancer Drugs: A Comprehensive Computational Investigation, *Organometallics*, 2024, **43**(19), 2172–2190.
23 H. Mina, A. Azadeh, A. Zatollah and Y. Bahman, Application of Nanoparticles for Efficient Delivery of Quercetin in Cancer Cells, *Curr. Med. Chem.*, 2024, **31**(9), 1107–1141.

24 M. Ferreira-Silva, C. Faria-Silva, M. C. Carvalheiro, S. Simões, H. S. Marinho, P. Marcelino, M. C. Campos, J. M. Metselaar, E. Fernandes, P. V. Baptista, A. R. Fernandes and M. L. Corvo, Quercetin Liposomal Nanoformulation for Ischemia and Reperfusion Injury Treatment, *Pharmaceutics*, 2022, **14**(1), 104–138.

25 R. G. R. Pinheiro, M. Pinheiro and A. R. Neves, Nanotechnology Innovations to Enhance the Therapeutic Efficacy of Quercetin, *Nanomaterials*, 2021, **11**(10), 2658–2684.

26 R. Sharma, P. Basist, A. Alhalmi, R. Khan, O. M. Noman and A. Alahdab, Synthesis of Quercetin-Loaded Silver Nanoparticles and Assessing Their Anti-Bacterial Potential, *Micromachines*, 2023, **14**(12), 2154.

27 E. M. Tomou, P. Papakyriakopoulou, E. M. Saitani, G. Valsami, N. Pippa and H. Skaltsa, Recent Advances in Nanoformulations for Quercetin Delivery, *Pharmaceutics*, 2023, **15**(6), 1656–1689.

28 M. J. Mitchell, M. M. Billingsley, R. M. Haley, M. E. Wechsler, N. A. Peppas and R. Langer, Engineering precision nanoparticles for drug delivery, *Nat. Rev. Drug Discovery*, 2021, **20**(2), 101–124.

29 M. K. Sah, B. Gautam, K. P. Pokhrel, L. Ghani and A. Bhattarai, Quantification of the Quercetin Nanoemulsion Technique Using Various Parameters, *Molecules*, 2023, **28**(6), 2540–2556.

30 S. Chen, Y. Lv, Y. Wang, D. Kong, J. Xia, J. Li and Q. Zhou, Tumor acidic microenvironment-responsive promodulator iron oxide nanoparticles for photothermal-enhanced chemodynamic immunotherapy of cancer, *ACS Biomater. Sci. Eng.*, 2023, **9**(2), 773–783.

31 D. Neri and C. T. Supuran, Interfering with pH regulation in tumours as a therapeutic strategy, *Nat. Rev. Drug Discovery*, 2011, **10**(10), 767–777.

32 H. Nakamura and K. Takada, Reactive oxygen species in cancer: Current findings and future directions, *Cancer Sci.*, 2021, **112**(10), 3945–3952.

33 X. He, Y. Deng, D. Ouyang, N. Zhang, J. Wang, A. A. Murthy, I. Spanopoulos, S. M. Islam, Q. Tu and G. Xing, Recent development of halide perovskite materials and devices for ionizing radiation detection, *Chem. Rev.*, 2023, **123**(4), 1207–1261.

34 R. Liu, Y. Chen, G. Liu, C. Li, Y. Song, Z. Cao, W. Li, J. Hu, C. Lu and Y. Liu, PI3K/AKT pathway as a key link modulates the multidrug resistance of cancers, *Cell Death Dis.*, 2020, **11**(9), 797.

35 M. E. Bahar, H. J. Kim and D. R. Kim, Targeting the RAS/RAF/MAPK pathway for cancer therapy: from mechanism to clinical studies, *Signal Transduction Targeted Ther.*, 2023, **8**(1), 455.

36 Z. Wang, J. Zhao, G. Wang, F. Zhang, Z. Zhang, F. Zhang, Y. Zhang, H. Dong, X. Zhao and J. Duan, Comutations in DNA damage response pathways serve as potential biomarkers for immune checkpoint blockade, *Cancer Res.*, 2018, **78**(22), 6486–6496.

37 Y. Zhou, S. Fan, L. Feng, X. Huang and X. Chen, Manipulating intratumoral Fenton chemistry for enhanced chemodynamic and chemodynamic-synergized multimodal therapy, *Adv. Mater.*, 2021, **33**(48), 2104223.

38 Y. Xu, Y. Guo, C. Zhang, M. Zhan, L. Jia, S. Song, C. Jiang, M. Shen and X. Shi, Fibronectin-coated metal–phenolic networks for cooperative tumor chemo-/chemodynamic/immune therapy via enhanced ferroptosis-mediated immunogenic cell death, *ACS Nano*, 2022, **16**(1), 984–996.

39 S. Naderlou, M. Vahedpour and D. M. Franz, Exploring the Role of Functional Groups in Modulating NO and CO Adsorption and Diffusion in 2D (Zn)MOF-470: A Multiscale Computational Study, *J. Phys. Chem. C*, 2023, **127**(38), 19301–19323.

40 R. Rajalakshmi and N. Ponpandian, Morphological design of $MnFe_2O_4$ facets (cube, flakes and capsules) for their role in electrical, magnetic and photocatalytic activity, *Mater. Res. Bull.*, 2023, **164**, 112242.

41 C. F. Macrae, I. Sovago, S. J. Cottrell, P. T. Galek, P. McCabe, E. Pidcock, M. Platings, G. P. Shields, J. S. Stevens and M. Towler, Mercury 4.0: From visualization to analysis, design and prediction, *J. Appl. Crystallogr.*, 2020, **53**(1), 226–235.

42 M. D. Hanwell, D. E. Curtis, D. C. Lonie, T. Vandermeersch, E. Zurek and G. R. Hutchison, Avogadro: an advanced semantic chemical editor, visualization, and analysis platform, *J. Cheminf.*, 2012, **4**(1), 17.

43 R. D. Dennington; T. A. Keith and J. M. Millam, *GaussView 5.0.8*, Gaussian, 2008.

44 W. Humphrey, A. Dalke and K. Schulten, VMD: visual molecular dynamics, *J. Mol. Graphics*, 1996, **14**(1), 33–38.

45 G. M. Morris, R. Huey, W. Lindstrom, M. F. Sanner, R. K. Belew, D. S. Goodsell and A. J. Olson, AutoDock4 and AutoDockTools4: Automated docking with selective receptor flexibility, *J. Comput. Chem.*, 2009, **30**(16), 2785–2791.

46 A. Bujacz, Structures of bovine, equine and leporine serum albumin, *Acta Crystallogr., Sect. D:Biol. Crystallogr.*, 2012, **68**(Pt 10), 1278–1289.

47 F. Neese, F. Wennmohs, U. Becker and C. Riplinger, The ORCA quantum chemistry program package, *J. Chem. Phys.*, 2020, **152**(22), 224108.

48 R. A. Kendall, T. H. Dunning Jr and R. J. Harrison, Electron affinities of the first-row atoms revisited. Systematic basis sets and wave functions, *Chem. Phys.*, 1992, **96**(9), 6796–6806.

49 C. M. Breneman and K. B. Wiberg, Determining atom-centered monopoles from molecular electrostatic potentials. The need for high sampling density in formamide conformational analysis, *J. Comput. Chem.*, 1990, **11**(3), 361–373.

50 C. I. Bayly, P. Cieplak, W. Cornell and P. A. Kollman, A well-behaved electrostatic potential based method using charge restraints for deriving atomic charges: the RESP model, *J. Phys. Chem.*, 1993, **97**(40), 10269–10280.

51 D.-L. Chen, A. C. Stern, B. Space and J. K. Johnson, Atomic Charges Derived from Electrostatic Potentials for Molecular and Periodic Systems, *J. Phys. Chem. A*, 2010, **114**(37), 10225–10233.

52 F. Zsila, Z. Bikádi and M. Simonyi, Probing the binding of the flavonoid, quercetin to human serum albumin by circular dichroism, electronic absorption spectroscopy and molecular modelling methods, *Biochem. Pharmacol.*, 2003, **65**(3), 447–456.
53 Z. Vaneková, L. Hubčík, J. L. Toca-Herrera, P. G. Furtműller, P. Mučaji and M. Nagy, Analysis of Binding Interactions of Ramipril and Quercetin on Human Serum Albumin: A Novel Method in Affinity Evaluation, *Molecules*, 2020, **25**(3), 547.
54 G. J. Quinlan, G. S. Martin and T. W. Evans, Albumin: biochemical properties and therapeutic potential, *Hepatology*, 2005, **41**(6), 1211–1219.
55 *The PyMOL Molecular Graphics System, Version 1.3*, Schrödinger: LLC.
56 E. F. Pettersen, T. D. Goddard, C. C. Huang, G. S. Couch, D. M. Greenblatt, E. C. Meng and T. E. Ferrin, UCSF Chimera--a visualization system for exploratory research and analysis, *J. Comput. Chem.*, 2004, **25**(13), 1605–1612.
57 J. Hutter, M. Iannuzzi, F. Schiffmann and J. VandeVondele, cp2k: atomistic simulations of condensed matter systems, *Wiley Interdiscip. Rev.: Comput. Mol. Sci.*, 2014, **4**(1), 15–25.
58 J. VandeVondele, M. Krack, F. Mohamed, M. Parrinello, T. Chassaing and J. Hutter, Quickstep: Fast and accurate density functional calculations using a mixed Gaussian and plane waves approach, *Comput. Phys. Commun.*, 2005, **167**(2), 103–128.
59 B. G. Lippert, J. H. Parrinello and P. Michele, A hybrid Gaussian and plane wave density functional scheme, *Mol. Phys.*, 1997, **92**(3), 477–488.
60 S. F. Boys and F. Bernardi, The calculation of small molecular interactions by the differences of separate total energies. Some procedures with reduced errors, *Mol. Phys.*, 1970, **19**(4), 553–566.
61 J. Contreras-García, E. R. Johnson, S. Keinan, R. Chaudret, J.-P. Piquemal, D. N. Beratan and W. Yang, NCIPLOT: a program for plotting noncovalent interaction regions, *J. Chem. Theory Comput.*, 2011, **7**(3), 625–632.
62 S. Mohapatra, *et al.*, Zeta potential and its role in colloidal stability of nanoparticles., *J. Nanomater.*, 2020, **2020**, 1–10.
63 J. Huang, *et al.*, Green synthesis of nanoparticles: A review of the role of plant polyphenols and flavonoids in nanoparticle formation, *Mater. Sci. Eng., C*, 2019, **96**, 107–115.
64 T. Gao, J. Lin, L. Xu and J. Guan, Self-adaptive flask-like nanomotors based on Fe_3O_4 nanoparticles to a physiological pH, *Nanomaterials*, 2022, **12**(12), 2049.
65 M. Shaghaghi, S. Rashtbari, S. Vejdani, G. Dehghan, A. Jouyban and R. Yekta, Exploring the interactions of a Tb(III)-quercetin complex with serum albumins (HSA and BSA): spectroscopic and molecular docking studies, *Luminescence*, 2019, **35**(4), 512–524.
66 F. Mohammadi, A. M. Bayan and A. W. Qarluq, Integrating molecular docking and molecular dynamics simulation approaches for investigation of the affinity and interactions of quercetin with Class D beta-lactamase, OXA-10, *Afr. J. Infect. Dis. Res.*, 2024, **2**(2), 19–26.